九州大学学術情報リポジトリ
Kyushu University Institutional Repository

In Situ Observation of Void Nucleation and Growth in a Steel using X-ray Tomography

Seo, Dowon
Department of Mechanical Engineering, Kyushu University

Toda, Hiroyuki
Department of Mechanical Engineering, Kyushu University

Kobayashi, Masakazu
Department of Mechanical Engineering, Toyohashi University of Technology

Uesugi, Kentaro
Japan Synchrotron Radiation Research Institute(JASRI)

他

https://hdl.handle.net/2324/4149937

出版情報：ISIJ International. 55 (7), pp.1474-1482, 2015-07-15. 日本鉄鋼協会
バージョン：
権利関係：© 2015 ISIJ

KYUSHU UNIVERSITY

ISIJ International, Vol. 55 (2015), No. 7, pp. 1474–1482

In Situ Observation of Void Nucleation and Growth in a Steel using X-ray Tomography

Dowon SEO,[1)*] Hiroyuki TODA,[1)] Masakazu KOBAYASHI,[2)] Kentaro UESUGI,[3)] Akihisa TAKEUCHI[3)] and Yoshio SUZUKI[3)]

1) Dept. of Mech. Eng., Kyushu Univ., Motooka 744, Nishi-Ku, Fukuoka, 819-0395 Japan.
2) Dept. of Mech. Eng., Toyohashi Univ. of Tech., Hibarigaoka 1-1, Toyohashi, Aichi, 441-8580 Japan.
3) Japan Synchrotron Radiation Research Institute, Mikazuki, Sayo, Hyogo, 679-5198 Japan.

(*Received on December 2, 2014; accepted on March 4, 2015*)

In situ synchrotron X-ray computed tomography has been applied to visualize and quantify the void nucleation, growth and coalescence leading to ductile fracture in a free-cutting steel. Uniaxial tensile test was performed and interrupted at different strain levels in order to understand the sequential damage process. Each void detected by the absorption contrast was sequentially tracked with increasing strain. Quantitative data obtained by this method was then used to compare and validate the several pre-existing models predicting the damage evolution. The gap between the void nucleation predictions and the experimental results was widened with increasing strain at high strain regime, because of the restrictive observation of voids and the void coalescence. The models predicting the void growth were also discussed with reassessing the constant α to take the reduction in equivalent diameter by nucleating voids.

KEY WORDS: ductile fracture; X-ray tomography; void nucleation; void growth.

1. Introduction

Ductile damage evolution is driven by plastic deformation which leads to the fracture of most metallic materials. It is well known that the basic mechanism of this ductile fracture involves three principal stages.[1)] The first stage consists of the nucleation of microvoids at the second-phase particles or at the interfaces between a matrix and them.[2–5)] The second stage consists of the growth of microvoids induced by the plastic stress and strain field. The third stage corresponds to the coalescence of the nucleated and grown voids which is resulted from the localization of the deformation and the interlinkages of the ligaments between adjacent voids. With technological advances in hardware and software of X-ray tomography technique, this final phenomenon can be clearly observed during in situ tensile test,[5–7)] as well as the first and the second stages.[8,9)]

Recently, many experimental and modeling efforts with X-ray tomography have been made to better understand and predict the void nucleation in steels as well as light metals such as aluminum alloys which can be more clearly observed due to their higher X-ray transmissivity than steels. Maire *et al.*[10)] measured the number of voids per unit volume in a dual-phase steel during in situ tensile test. The acquired quantitative data has then used to validate a model of void nucleation based on the Argon criterion.[11)] It has been shown that the number of voids related to the local true strain and increased very strongly after necking. The critical value of strain which nucleation start from depends on the stress triaxiality. Landron *et al.*[12)] obtained similar results and identified ε_{N0} as the strain with the first occurrence of nucleation for the smooth and the notched samples of the dual-phase steels. They revealed two different nucleation regimes at low and high strains and proposed the empirical equation modified the Argon criterion by using the local stress triaxiality for interface decohesion in the dual phase. Bareggi *et al.*[13)] compared the evolution of the void number in the different shape of samples to study the effect of stress triaxiality on the evolution of damage. They revealed that the samples which have a higher value of stress triaxiality show a higher value of nucleation, and the nucleation in the soft matrix such as pure ferrite was particularly low. Fabregue *et al.*[9)] also carried out comparative study on the damage evolution in two homogeneous steels. Four serial studies on the nucleation mentioned above, however, were concentrated on the nucleation by decohesion at the interfaces between dual phases or at grain boundaries without considering the effect of the inclusions or the particles which are regarded as having a predominant role in the damage evolution.[11)]

Many damage models focus on void growth. Early growth models began to germinate from simple analytical approaches for isolated voids in a perfectly plastic infinite matrix, *e.g.*, McClintock model for cylindrical void,[14)] Rice and Tracey (RT) model for spherical voids.[15)] The latter model has been widely used to predict damage growth with X-ray tomography.[13)] Weck *et al.*[6)] analyzed the void growth in copper and Glidcop containing artificial array of holes oriented at an arbitrary angle to the tensile axis and

* Corresponding author: E-mail: seodwn@gmail.com
DOI: http://dx.doi.org/10.2355/isijinternational.55.1474

© 2015 ISIJ

demonstrated that the RT model gives good predictions for growth of quasi-spherical voids with stress triaxiality variation. Bouaziz *et al.*[16] and Marie *et al.*[10] proposed the modification of the RT model in order to account for mismatch between the prediction and the experimental measurement resulted from nucleation at high strain regime. The RT model was later revised by Huang[17] in order to extend the approach to low values of stress triaxiality. This model has been demonstrated good agreement on various types of steels and extended by subsequent studies to take into account the shape change of voids in tensile and transverse directions using a finite number of voids in different types of steels such as austenitic, ferritic and martensitic matrices.[9,18]

Most studies mentioned above are limited to the inclusion-free or unconsidered,[10,12,13,18] the homogeneous[9] and the model materials embedding artificial damages[6,7,19,20] for easy estimation. Concerning the complexity of damage evolution leading to a ductile fracture, the artificial voids have been employed in many studies to simplify the analysis of damage evolution. However, an eager desire to observe the void growth in the commercial steels is still remained, as well as the void nucleation. The quantitative data on the damage evolution of the entire void population, in particular, is valuable to making the failure predictions more accurate.

In this work, the damage evolution in a steel including soft particles was studied in situ by combined a tensile test and the tomographic observation to better understand the nucleation and growth events of voids during ductile deformation. Synchrotron X-ray absorption tomography, one of the most reliable experimental techniques available, has been applied to visualize and collect quantitative three-dimensional (3 D) information on the damage evolution. Quantitative data obtained by this method was then used to compare and validate the several pre-existing models predicting the damage evolution.

2. Experimental Procedure

2.1. Material

A commercial free-cutting steel, JIS SUM24L which has a chemical composition (wt.%) of 1.1 Mn, 0.32 S, 0.28 Pb, 0.08 C, 0.075 P and balance Fe was used in this study. Soft inclusions such as manganese sulfides (MnS), which are added to ferrite matrix to enhance the machining performance, were elongated in rolling direction (RD) of an extruded rod, as shown in **Fig. 1**. From the etched microstructure of SUM24L sample, the MnS inclusions were not uniform in size as well as in their spatial distribution. The ferrite grains of about 50 μm as main matrix and the pearlite second phases which stretched and oriented to RD were observed. Leads (Pb) were also detected around tails of some MnS inclusions (14.2% of entire MnS inclusions) by EDX analysis, as shown in **Fig. 2**. The influence of Pb particle on damage evolution was not considered in this study because of its low volume fraction of only 0.02%. It would be appropriate to regard the Pb particles as a minor factor in damage evolution compared to the MnS inclusions. As can be seen in Figs. 1 and 2, some MnS inclusions were broken into pieces caused by sample preparation and manufacturing process. It was confirmed through tomograms that

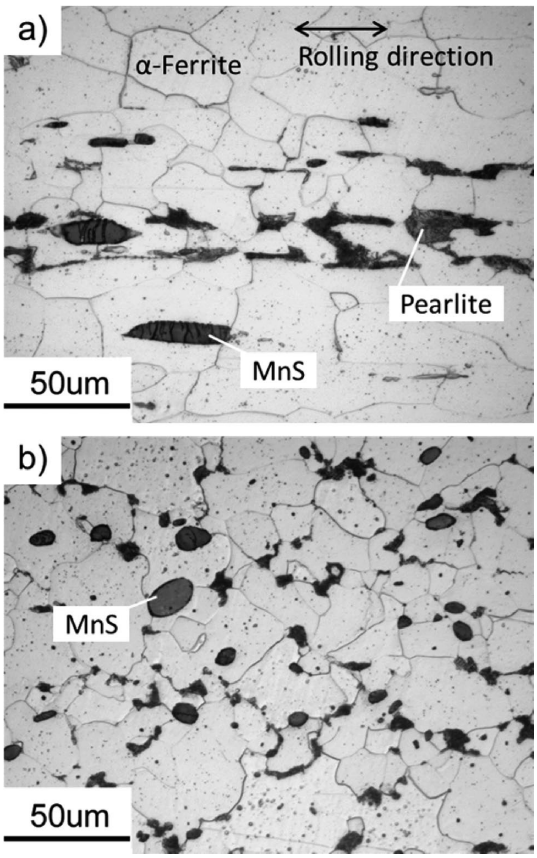

Fig. 1. Optical micrographs of the free-cutting steel in a) TD and b) RD. MnS inclusions appear in elongated particles, ferrite in light gray and pearlite in dark gray.

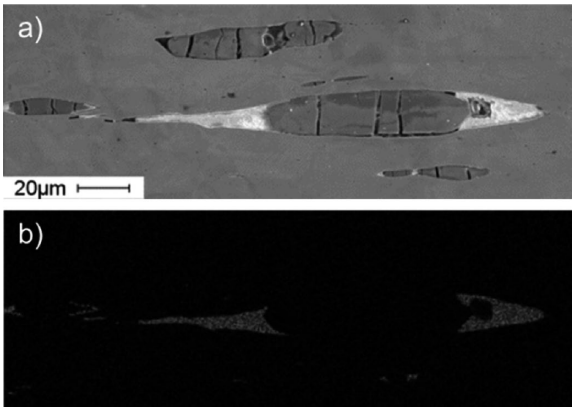

Fig. 2. MnS inclusions with Pb tails embedded in matrix; a) SEM image and b) Pb in EDX mapping.

there were pre-existing cracks on several MnS inclusions in an as-received specimen. The volume fraction and average diameter of the MnS were found to be about 1.1% and 8.3 μm, respectively.

2.2. In Situ Tensile Test

A flat tensile specimen of 600 μm in thickness was machined from the round bar of 25 mm in diameter, where the applied loading axis to be corresponded to RD. Nominal dimension of gauge cross section was 600×600 μm^2. Then, the specimen was carefully mounted on hydraulic snubbing rigs of a testing machine. Tensile test was performed at constant displacement rate (CHS$=$0.0005 mm/s) at room temperature using a specially designed in situ testing machine

© 2015 ISIJ

installed on a highly precise rotation stage described in the references.[21,22] X-ray transparent tube was used to transmit the load between the upper and lower grips of the machine. During the in situ experiments, the samples are deformed in tension and the test interrupted at different strain levels (10 steps up to the strain of 64%) with planned interval in order to acquire tomograms sequentially, as shown in **Fig. 3**.

For a more accurate estimation of the true strain in the specimen, the area A_{min} of the minimal cross section perpendicular to the tensile axis z was measured from the tomographic images. This value was independent of the z position along the length of specimen before the onset of necking. After necking, the sectional area varied along z axis and was used to calculate the true strain ε in the minimal cross section at each deformation step. It has been assumed that the strain was constant in each slice perpendicular to the tensile axis z. This assumption could not be verified after necking, rather it was used here as a reasonable approximation for an average value of the true strain in the minimal cross section. The volume change of the specimen due to the void evolution was neglected in this calculation, because it always remains smaller than 3.5% in total. In combination with the load P, A_{min} was also used to calculate the true stress σ in the narrowest cross section of the neck at each deformation step.

2.3. X-ray Tomography

X-ray tomography experiment was conducted at the undulator beamline BL20XU of SPring-8, Japan Synchrotron Radiation Research Institute. A monochromatic X-ray beam of 40 keV, which is produced by a liquid nitrogen-cooled Si (511)-(333) double crystal monochromator, was applied with a beam source-to-sample distance of 80 m. A sample-to-detector distance was set to 65 mm in order to apply an absorption contrast imaging. A cooled 2D-CCD image sensor (C4880-41S, Hamamatsu Photonics, Japan) of 4 000×2 624 pixels was used in 2×2 binning mode for acquiring transmitted X-ray images through a 10 μm thick scintillator of Lu_2SiO_5:Ce (LSO) and a ×20 objective lens. The effective field of view was about 720×600 μm. 1 500 radiographs were recorded for one scan by scanning 180° with 0.12° step. Isotropic voxels with 0.5 μm edges were obtained in the tomographic volumes reconstructed from 2 D projection radiographs via the convolution back projection algorithm.

The stack of slice images reconstructed with a 16-bit gray depth which corresponds to the linear absorption coefficient (LAC) of the material inside sample was converted into 8-bit image in order to reduce the data size and the processing time in sequential analysis. The LAC profile of the sample was continuously distributed over a wide range of values from –8 to 61 cm^{-1}. It was distributed up to the negative range due to the effect of X-ray phase contrast coming from a slightly long sample-to-detector distance which was applied in this study to enhance the spatial resolution based on the previous experiment.[23] The LAC was also used to determine the lower and upper thresholds for segmenting out the inclusions and the voids in the matrix after 8-bit conversion, as shown in **Fig. 4**. After the segmentation process, 3D volumetric image was rendered to evaluate a spatial distribution of the inclusions and the voids by using commercial volumetric graphic software.

The tomography technique enables in situ observation of time dependent evolution of the voids during deformation by tracking the internal microstructural features.[24,25] First, tomographic volume image was provided into image processing to find the position, the volume and the surface area of the voids. The home-made software written by the Matlab was used for this quantitative image analysis. The region of interest (ROI) of 696 μm (W)×726 μm (D)×548 μm (H) at final step of tomography scan

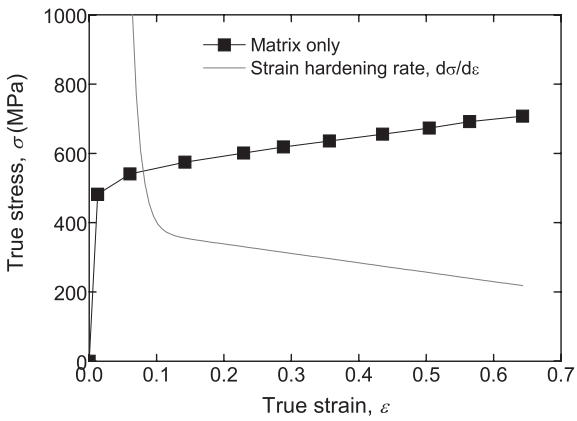

Fig. 3. True stress and strain hardening rate curves as a function of true strain. Tomographic scan was performed with planned interval during in situ tensile test. Marks on the curve represent the scan points.

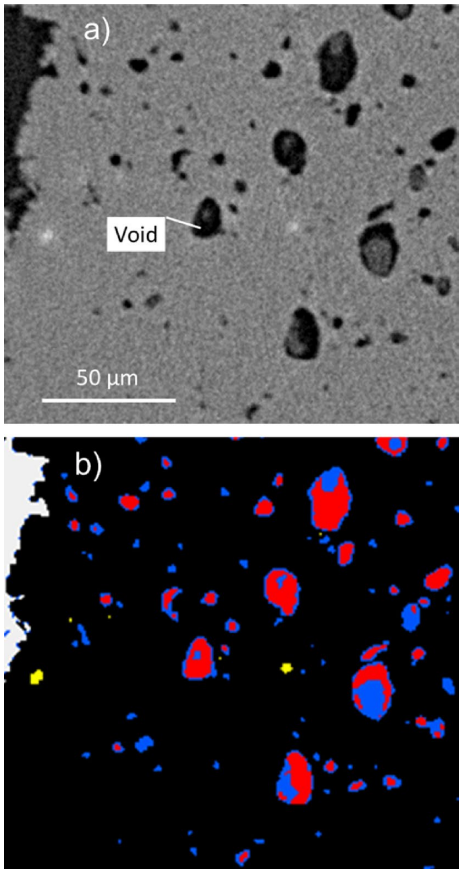

Fig. 4. Sectional view of sample a) before and b) after segmentation by LAC of the inclusions and voids. Red indicates voids, blue MnS, yellow Pb and black a matrix. (Online version in color.)

© 2015 ISIJ

($696\times726\times332$ μm^3 at unloading state) was cut off from the center of the stack of slice images. The cut images were converted into binary images. The upper threshold value of LAC=18 cm^{-1} was chosen for segmentation taking the LAC of the voids (LAC=–8 to 18 cm^{-1}) and the matrix (LAC=19 to 45 cm^{-1}) into account. A 3D labeling algorithm was applied to the binarized images. After labeling all voids, the position of gravity center, the volume and the surface area of them were measured applying the marching cube algorithm that gives pentagonal faceted isointensity surface.[26] Considering the resolution of the tomography, the voids that consist of fewer than 8 voxels were eliminated from further quantitative analysis. Over four thousands voids and inclusions were observed in the ROI region and were tracked with an increase of tensile strain.

Before the microstructural tracking of two data sets containing sequential tomographic observation, an image registration process is necessary because of a localized translation and rotation of target objects during deformation. The registration was made by introducing an algorithmic routine with a transformation matrix which was calculated from the eight sets of the tracking object pairs in the two sequential data by minimizing the sum of distance difference between corresponding pairs. It was difficult to find the matching object pairs correctly due to inhomogeneous deformation and variation of image quality. Therefore, a matching probability parameter, M_p was introduced to suppress tracking errors,

$$M_p = \alpha L_{ij} + \beta S_{ij} + \gamma V_{ij} \quad \text{..... (1)}$$

where, L_{ij}, S_{ij} and V_{ij} are the parameters in location, surface area and volume of the objects, respectively. α, β and γ are processing weights for three parameters, where $\alpha+\beta+\gamma=1$. The subscripts i and j denote the index numbers that are assigned in the labelling process. The details of the matching algorithm are described in the reference.[24,25] In this study, the threshold values of M_p^{th1} and M_p^{th2}, which are parameters verifying the validity of the object pair matching, set to 0.8 and 0.1, respectively. The weight parameters, $\alpha:\beta:\gamma =$ 0.8:0.1:0.1 were also used.

3. Results and Discussion

3.1. Tensile Behavior and Triaxiality

Tensile behavior was monitored in situ during the X-ray tomography experiment and the stress-strain curve obtained is given in Fig. 3. This curve was calculated by using the minimal cross section of the specimen at each strain step, thus the stress values were higher than macroscopic nominal strengths as well as the strains since they referred to local values concentrated in the cross section. For instance, the ultimate stress and the elongation were 540.7 MPa (at $\varepsilon=0.06$) and 64.3%, respectively, while they were approximately 420 MPa and 30% in macroscopic nominal values. It shows yield strength of 482.3 MPa and then exhibits a relatively low strain hardening up to maximum strength compared to other steel grades such as austenitic 316 L steel.[9] The fracture surface of the specimen was also observed using SEM and represented a typical ductile fracture with many dimples of different sizes surrounding broken inclusions, as shown in **Fig. 5**. Deep dimples observed on the fracture surface are thought to originate in the voids grown or coalesced during deformation.[10] The coalescing ligament of about 19 μm at the longest and the grown voids in the diameter range of 1 to 21 μm were observed at the cross section of the final crack propagation.

After some deformation, the stress triaxiality T may evolve if the geometry of the specimen changes. With the evolution of the cross section along z axis, the curvature radius of outer surface r at the narrowest cross section of the specimen and the radius of this cross section w can be used to calculate the evolution of the triaxiality in the center of the necked specimen using the Bridgman approximation.[27] It is often used in the tomographic study as a first-order estimation of the triaxiality regardless of the specimen geometries, *e.g.*, cylindrical bars,[5,8,12,18] flat ones,[6,7,9,10,13,19,20] even at notched ones.[5,8,13,18,20] The Bridgman formula, however, is only valid for an axisymmetric geometry. It seems relatively acceptable in the case of the cylindrical specimen, and then the radius r could be measured using an external shape of the specimen with assuming that each cross section is a circle at each deformation step. In the case of square geometry such as the flat specimens, this is a crude estimation and the triaxiality calculated with this manner should be reconsidered.

Replacing the stress distribution in three components (radial, tangential and axial stresses derived by Bridgman) into the von Mises yield function and vanishing shear stress term in it, the equivalent stress σ_{eq} can be presented as follows;[27,28]

$$\sigma_{eq} = \frac{\sigma_m}{\left(1+\frac{2r}{w}\right)\ln\left(1+\frac{w}{2r}\right)} = \sigma_m \zeta\left(\varepsilon\right) \quad \text{..... (2)}$$

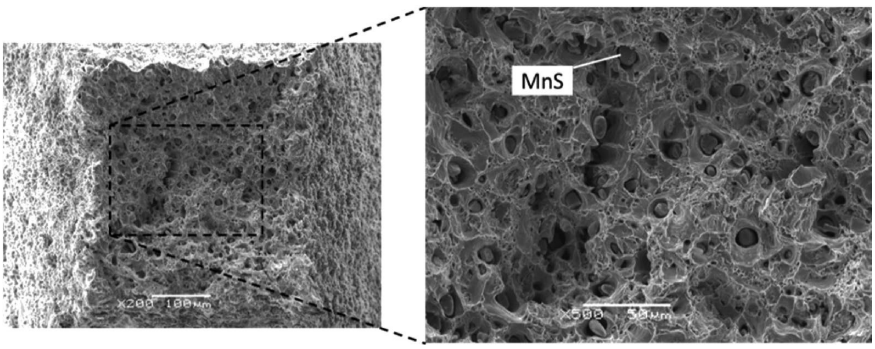

Fig. 5. SEM fractographs of the specimen showing deep dimples circumferential broken inclusions.

© 2015 ISIJ

where, σ_m is the average stress and the necking correction parameter $\zeta(\varepsilon)$ should always be smaller than 1.0 after onset of necking. Because of the difficulties in measuring three components of stress after onset of necking, Bridgman's stress correction in Eq. (2) has been considered to give reliable approximation.[29] It is generally accepted that if r and w are accurately measured, the stress-strain relation can be predicted beyond necking fairly well in a specimen with a circular cross section. Only if diffuse necking is considered, an empirical expression for the neck geometry parameter introduced by LeRoy[30] could be helpful to simplify calculating r and w which are both difficult to measure with sufficient degree of accuracy, especially in the case of the specimen with square section;[31]

$$\frac{w}{r} = 1.1\left(\varepsilon - \varepsilon_{Pmax}\right) \quad \text{..... (3)}$$

where, ε_{pmax} implies the true strain when an applied load reaches a maximum value. In order to reduce the possible errors induced by above hypothesis, the Choung's formula[28] which was proposed for the flat specimen with square cross section was also considered in this study. Recalling Eq. (2), the equivalent true flow stress σ_{eq} was calculated using the correction parameter $\zeta(\varepsilon)$ as follows;[28]

$$\zeta\left(\varepsilon\right) = \begin{cases} 1 & for\,\varepsilon < 1.4n \\ \alpha\varepsilon^2 + \beta\varepsilon + \gamma & for\,\varepsilon > 1.4n \end{cases} \quad \text{..... (4)}$$

$$\begin{aligned} \alpha &= -0.0704n - 0.0275 \\ \beta &= 0.4550n - 0.2926 \\ \gamma &= 0.1592n + 1.024 \end{aligned} \quad \text{..... (5)}$$

$$n = \frac{d\ln\sigma}{d\ln\varepsilon} \quad \text{..... (6)}$$

where, n is the strain hardening exponent measured from the slope of $\ln\sigma$-$\ln\varepsilon$, and was 0.14 after the onset of localized necking. This formula can be available with knowledge of the hardening exponent and incremental plastic strain values which are determined by in situ tensile test. **Figure 6**(a) shows variation in the correction parameter ζ as a function of true strain calculated by Eqs. (4) and (5). Figure 6(b) shows the evolution of stress triaxialities in the minimal section during in situ tensile test which was calculated by LeRoy's and Choung's formulas. These calculated values will be used in the void nucleation and growth models which will be discussed in more detail in subsequent sections. The evolution in both triaxialities was mainly controlled by the plastic strain. The triaxiality calculated by LeRoy's formula showed a linear increase with increasing strain, but in the case of calculating by Choung's formula, the triaxiality remained constant up to a strain of 0.14 and was equal to 1 according to Eq. (4). This is based on the assumption that the triaxiality does not vary before necking appears. Then a large increase in triaxiality was observed. Both triaxialities grew over 1.1 at failure that corresponds to relatively high triaxiality compared to that of tensile specimens of ordinary sizes. It may be due to tiny specimen geometry used in this study such as a gauge length of 400 μm and a curvature radius of 2 mm.

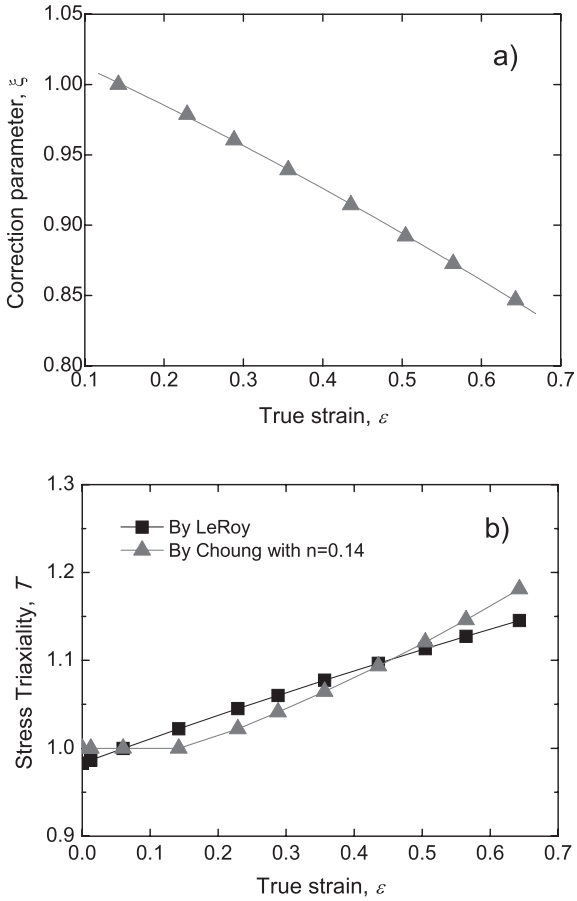

Fig. 6. Variation in a) necking correction parameter and b) stress triaxiality as a function of true stress.

3.2. Void Nucleation

Nucleation occurred during entire deformation process in a continuous manner. **Figure 7** shows the evolution of the number of voids in a unit volume as a function of the true strain. From experiment, the number density of voids N increased slightly with increasing strain at the beginning of the tensile deformation and the plateau was observed near the fracture. A slight suppression of the N at high strain regime could be due to a high occurrence of void coalescing. A considerable number of voids nucleated at that regime could be coalesced into the neighboring void clusters in a short period of time as soon as they nucleated, then it might be failed to acquire all of them at the specified interval of the tomography scan. The predicting model for nucleation based on the Argon criterion[11] was considered to verify its validation with this experimental result and could be described by an exponential expression of the following form:[10,12,13]

$$N = A\frac{\varepsilon}{\varepsilon_N} exp\left(\frac{\varepsilon}{\varepsilon_N}\right) + N_0 \quad \text{..... (7)}$$

$$\varepsilon_N = \varepsilon_{N0} exp\left(-T\right) \quad \text{..... (8)}$$

where, A is a constant equal to 9 000 mm^{-3} in this study and ε_N is a critical value of the strain from which nucleation starts to occur. ε_{N0} is the critical strain when a pure shear is applied and a value of 0.94 seems to allow a good fit for the evolution of N measured in this study. In order to take the number of pre-existing voids into account,

© 2015 ISIJ

N_0=56 296.8 mm^{-3} was additionally adopted which was observed by tomography. In the early stage of strain, both predictions, calculated with LeRoy's and Choung's, T were in close agreement with the experimental data observed by tomography. Beyond ε=0.44, however, the gap between two predictions and the experimental results was widened with increasing strain, thus the predicted values were almost double of the experimental result at a point just before fracture. Even though considering the other prediction modified by Landron *et al.*,[12] it is easily expected that this mismatch could still be remained due to its limited validation. Thus these predictions could be valid only for the very beginning of the deformation ($\varepsilon/\varepsilon_N$<1) at which no void coalescence occurs.[10,12]

These big mismatches in two predictions seem to be originated from the restrictive observation, *i.e.*, these predictions considered the number density of voids only in partial volumes of their specimens selectively, especially excluding the coalescing event. The decrease in the number of nucleating voids at high strain regime could be directly related to high occurrence frequency of void coalescence (the number of occurrence of void coalescing events per unit volume). It could also be explained in part by the voids appearing at the MnS inclusions. Void nucleation is often inhomogeneous and occurs either by inclusion fracture, by separation of the inclusion/matrix interface or by cavitation at the matrix.[12] However, the voids nucleated at the inclusions (by the inclusion fracture or by the interface separation) were neglected in the experimental measurement due to the technical difficulty of segmentation. It was difficult to identify the voids from the MnS inclusions when they were connected because their LAC values overlapped each other.

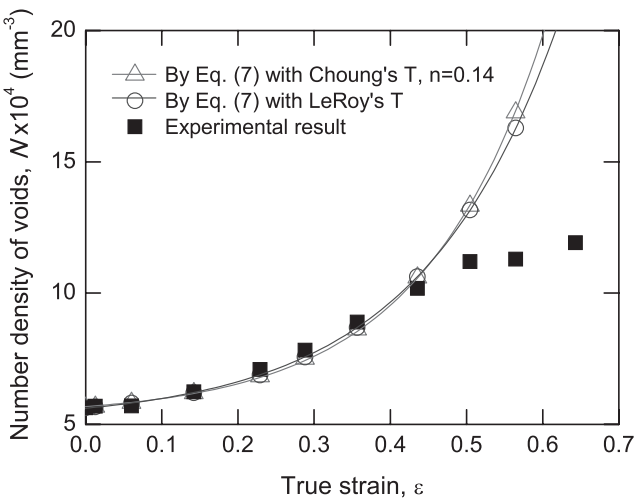

Fig. 7. Evolution of number density of voids by experimental measurements and two predictions as a function of true stress.

3.3. Void Growth

Figure 8 shows the typical evolution of the reconstructed vertical section of the ROI. These sections were extracted from the tomographic 3D block at each strain and had selectively chosen to show the growth of voids in same plane. As can be seen, some voids seem to disappear from the 2D sections at subsequent strains due to their relative translocations with ductile deformation. This issue, however, can be solved by 3D observation and the matching algorithm which was previously discussed. The voids are black in color and the inclusions are dark grey in the light grey matrix. A large number of voids oriented parallel to the tensile axis were observed inside ROI. The formation of voids was concentrated at the interface between inclusions and matrix, or at the crevice of the inclusions broken into pieces after tensile deformation. The necking started to occur around a strain of 0.23 shown in Fig. 8(b).

The volume of each void was measured and its equivalent diameter was then calculated assuming that it would be spherical or near spherical in shape. Overall volume of the entire void population in the ROI was increased with increase of the strain, as shown in **Fig. 9**(a). The average equivalent diameter of the entire voids, however, was decreased at the high strain regime which was contrary to expectation from Fig. 8. Similar phenomena were

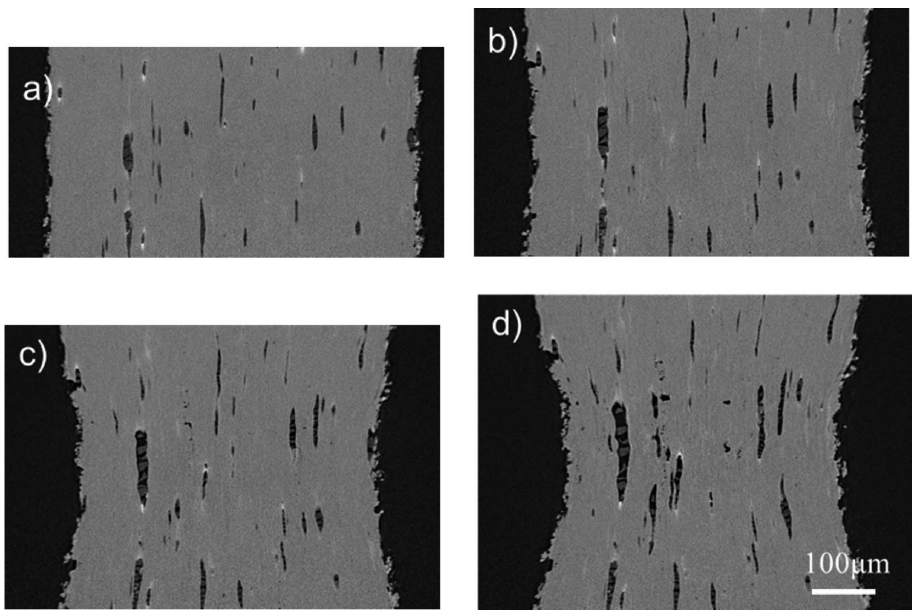

Fig. 8. Reconstructed tomographic slice images showing void growth at strain of a) 0, b) 0.23, c) 0.50 and d) 0.64.

© 2015 ISIJ

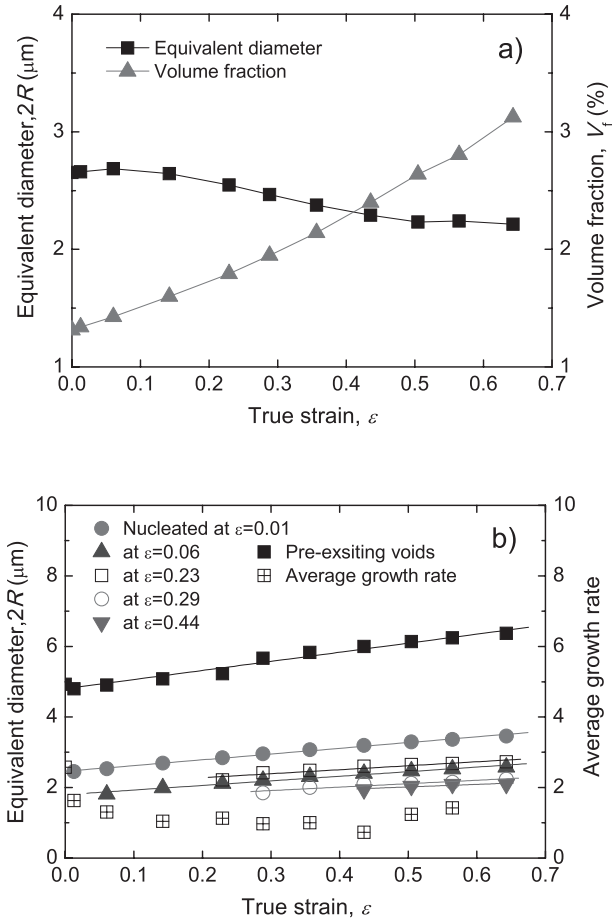

Fig. 9. Evolution of average equivalent diameter of a) entire voids and b) voids nucleating at various strains.

observed in several previous works with different types of steels.[9,10,13,18] The average diameter was almost constant or quasi-stagnated in their works when the entire voids were taken into account.[9,10] A reduction in the equivalent diameter of the voids could be due to the nucleation of the voids in the matrix. X-ray tomography allows the separation of the nucleating voids from the growing voids and leads to a better understanding of this phenomenon.

Figure 9(b) shows the evolution of the average equivalent diameter of the voids which were pre-existed before tension (*i.e.*, voids originating from the inclusions) and nucleated at each strain (*i.e.*, voids from the matrix). The average growth rates of the voids pre-existed at $\varepsilon=0$ and nucleated at each strain (from $\varepsilon=0.01$) were also obtained by calculating the evolutionary slope of the void diameters with strain, based on the linear least squares regression. A limited number of the voids, those traceable over the whole deformation process by the matching algorithm described in the section 2.3, were selected from the entire voids as shown in Fig. 9(a), in order to make the qualitative outcome analysis to be more reliable. For instance, 94.6% of the entire pre-existing voids and 74.6% of the entire voids nucleating at the strain of 0.01 were traced up to a fracture. It is believed that the number of traced voids is adequate to make a valid generalization about void nucleating effect.

In the case of the pre-existing voids, the equivalent diameter increased with increasing strain and ranged from 4.8 to 6.4 μm during all the deformation process. It was relatively large compared to the other series of the voids nucleation at each strain step. The diameter of the pre-existing voids almost doubled one of the nucleating voids just before fracture ($\varepsilon=0.64$). The voids nucleating at each strain, by contrast, were in the diameter range of about 1.8–2.5 μm. In the process of calculating the average diameter of the entire void population, it is reasonable to assume that the growth in the diameter of the pre-existing voids is counter balanced by the small diameter of the freshly nucleated voids. In order to cover this matter, the initial diameter of the pre-existing voids such as the inclusions also has to be taken into account together with the number of them. In the case that the defects or the inclusions inside sample are relatively large, the damage could be underestimated through this numerical averaging.

On the one hand, it is notable that the growth rate of the pre-existing voids was slightly higher than those of the other series of the voids nucleating at each strain, as shown in Fig. 9(b). The former was 2.58, while the latter was in the range of 0.73–1.63. The soft MnS inclusions can be the initiation site of the void nucleation at the early stage of the ductile deformation.[32] It should be noted that in this study, the MnS inclusions were considered as the pre-existing voids because of their considerably low strength and deformation resistance compared to the ferrite matrix, in order to simplify the evaluation of the damage evolution. On the other hand, the growth rate of the voids nucleated from the matrix was slightly decreased with increasing of nucleated strain because of strain hardening effect. Over the strain of 0.50, however, a slight increase in the growth rate was observed and that could be due to an extensive coalescing of voids at high strain regime.

A modelling effort to develop an adequate prediction of the void growth was attempted including comparison with several existing models to validate them. The RT model, a simplest and oldest analytical approach, has been widely used to predict the void growth.[6,10] It predicts the growth of an initially spherical void in a rigid and infinite, perfectly plastic matrix subjected to a homogeneous strain field.[15] Assuming a fully isotropic void growth, the RT model predicts an exponential relationship between the average growth rate of voids and the increment in equivalent plastic strain as follows:

$$\frac{dR}{d\varepsilon_{eq}} = \alpha_{RT}\, exp\left(\frac{3}{2}T\right)R \quad \text{..... (9)}$$

where, α_{RT} is a constant and R is the average equivalent radius of voids. The growth in void radius is mainly governed by the triaxiality T level.[15,17] A value of $\alpha_{RT}=0.283$ which was first computed by RT was later modified by Huang[17] to extend the estimation to low values of T:

$$\frac{dR}{d\varepsilon_{eq}} = \alpha_{H}\, exp\left(\frac{3}{2}T\right)R \quad \text{..... (10)}$$

$$\begin{aligned} \alpha_H &= 0.427\, T^{1/4} && \text{for } T < 1 \\ \alpha_H &= 0.427 && \text{for } T \geq 1 \end{aligned} \quad \text{..... (11)}$$

First, these two models were employed to fit the experimental measurement of the average equivalent diameter, as shown in **Fig. 10**. The values of T and ε_{eq} used here were

© 2015 ISIJ

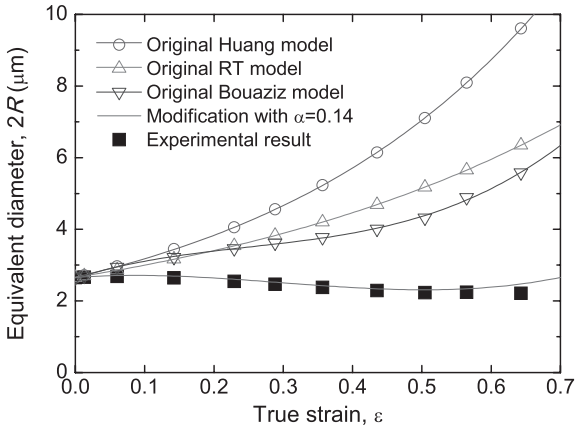

Fig. 10. Comparison between experimental measurement of average equivalent diameter of voids and various prediction models.

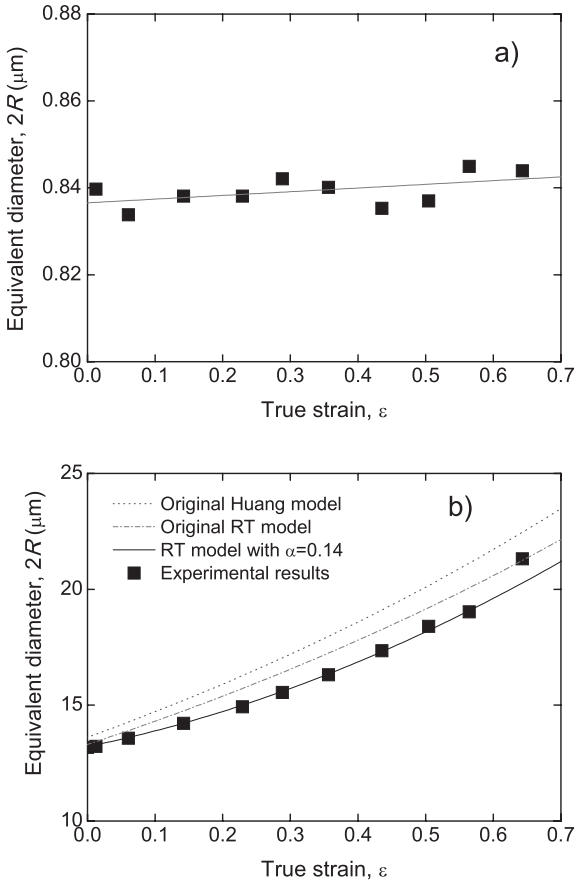

Fig. 11. Evolution of the average equivalent diameter of a) the 50 smallest voids nucleating at each strain and b) the 20 largest voids.

experimentally measured in the previous section 3.1 and shown in Fig. 6(b). Two simple fits using the pre calculated values of α let to a discrepancy between the measured and the calculated evolution of R because α_{RT} and α_H were computed for isotropic growth in a perfectly plastic matrix. The strain hardening of the matrix also could reduce the prediction of these types of models.[33] Meanwhile, there were several reports demonstrating that the evolution of R was in fair agreement with two models in case of calculating with a limited number of the relatively large voids which were only concerned with growth[8–10,13,18] and replacing the initial value of α by a specific constant depending on a material and T state allowed them to be more valid.[9,18] These two items seem to be valuable for making the prediction better.

Furthermore, the sequential nucleation of the voids should also be taken into account in order to describe the evolution of the average diameter of the entire void population. Because, the tiny voids nucleating at following deformation process tend to reduce the numerical average value of the diameter as mentioned previously. In order to cover this issue, it is reasonable that the number fraction of each type of voids, *i.e.*, the pre-grown and the freshly nucleating voids at each strain, should additionally be considered as follows:

$$\frac{dR}{d\varepsilon_{eq}} = \frac{d}{d\varepsilon_{eq}}\left(\frac{R_g N_g}{N}\right) + \frac{d}{d\varepsilon_{eq}}\left(\frac{R_n N_n}{N}\right) \quad \text{..... (12)}$$

where, two subscripts following R and N in the right-hand side (RHS) of Eq. (12), g and n refer to the growing and the nucleating voids, respectively. This approach was proposed by Bouaziz *et al.*[34] with modifying Eq. (10) and the average radius of voids was given by:

$$\frac{dR}{d\varepsilon_{eq}} = \alpha_H \, exp\left(\frac{3}{2}T\right)R - \frac{1}{N}\frac{dN}{d\varepsilon_{eq}}\left(R - R_0\right) \quad \text{..... (13)}$$

where, R_0 is the equivalent radius of the voids at nucleation and is assumed to be constant. As can be shown in Fig. 10, however, this model still overestimated the growth along with RT and Huang models. This discrepancy in the growth could be explained by a small proportion of the nucleating voids to the entire voids for overall deformation process, *e.g.*, the nucleating voids was only 12% of the entire void population at ε=0.36. In addition, the size of the nucleating voids was extremely small, as a courtesy of the enhanced resolution of the tomography used.

Concerning this matter, the value of R_0 in Eq. (13) was reassessed by calculating the average equivalent radius of the 50 smallest voids at each strain and was almost constant equal to 0.42 μm, as shown in **Fig. 11**(a). The first item in RHS of Eq. (13) used to estimate the void growth was also replaced with the RT model instead of the Huang model, because the values predicted by RT model were more close to the experimental data, as shown in Fig. 10. The original value of constant α_{RT} was reconsidered with a view to improving the growth prediction. It was calculated using the 20 largest voids at each strain step and the best fit was when α=0.14 was substituted for the α_H in RHS of Eq. (13), as shown in Fig. 11(b). As can be seen in Fig. 10, this modification is in relatively good agreement with the experimental results even though it overestimates slightly at higher strain regime. The mismatch at high strain could be due to the extremely high occurrence of void clustering which was not taken into account in this approach.

4. Conclusion

Void nucleation and growth leading to ductile fracture in free-cutting steel were successfully visualized and quantified using an in situ high resolution synchrotron X-ray computed tomography. Several models of void evolution were validated and discussed based on quantitative observation as follows.

The empirical equation for the geometric parameters

© 2015 ISIJ

of necking induced by LeRoy was adopted to calculate the stress triaxiality of the specimen with square section and gave more accurate prediction of void nucleation than Choung's formula. Based on tomographic observation, the gap between the void nucleation predictions and the experimental results was widened with increasing strain beyond $\varepsilon=0.44$, because of the restrictive observation of voids and the coalescing event of voids at high strain regime. Wide discrepancies were observed between the measured and the predicted evolution of void diameters even by the Bouaziz modification considering the reduction in the numerical average value of diameter resulted from void nucleation. With modified constant $\alpha=0.14$, the Bouaziz model gave a good agreement with tomographic observation even though it overestimated slightly at high strain regime due to extremely high occurrence of void clustering.

Acknowledgments

Authors gratefully acknowledge that this work was undertaken as a technical research aid project "Breakthrough in research on steel by realizing 4D imaging" of the ISIJ Innovative Program for Advanced Technology. Authors would like to express thanks to Mr. K. Kawakami (Graduate School of Eng., Toyohashi Univ. of Tech., Japan) for his assistance with tomography experiments and data analysis in part.

REFERENCES

1) P. F. Thomason: *J. Inst. Met.*, **96** (1968), 360.
2) L. Babout, E. Maire, J. Buffiere and R. Fougeres: *Acta Mater.*, **49** (2001), 2055.
3) L. Babout, E. Maire and R. Fougeres: *Acta Mater.*, **52** (2004), 2475.
4) E. Marie, C. Bordreuil, L. Babout and J. C. Boyer: *J. Mech. Phys. Solids*, **53** (2005), 2411.
5) A. Weck, D. S. Wilkinson and E. Maire: *Mater. Sci. Eng. A*, **488** (2008), 435.
6) A. Weck, D. S. Wilkinson, E. Maire and H. Toda: *Acta Mater.*, **56** (2008), 2919.
7) A. Hosokawa, D. S. Wilkinson, J. Kang, M. Kobayashi and H. Toda: *Int. J. Fract.*, **181** (2013), 51.
8) E. Marie, S. Zhou, J. Adrien and M. Dimichiel: *Eng. Fract. Mech.*, **78** (2011), 2679.
9) D. Fabregue, C. Landron, O. Bouaziz and E. Marie: *Mater. Sci. Eng. A*, **579** (2013), 92.
10) E. Marie, O. Bouaziz, M. D. Michiel and C. Verdu: *Acta Mater.*, **56** (2008), 4954.
11) A. S. Argon, J. Im and R. Safoglu: *Metall. Trans. A*, **6** (1975), 825.
12) C. Landron, O. Bouaziz, E. Marie and J. Adrien: *Scr. Mater.*, **63** (2010), 973.
13) A. Bareggi, E. Maire, O. Bouaziz and M. D. Michiel: *Int. J. Fract.*, **174** (2012), 217.
14) F. A. McClintock: *J. Appl. Mech.*, **35** (1968), 363.
15) J. R. Rice and D. M. Tracey: *J. Mech. Phys. Solids*, **17** (1969), 201.
16) O. Bouaziz, E. Maire, M. Giton, J. Lamarre, Y. Salingue and M. Dimichiel: *Metall. Res. Technol.*, **105** (2008), 102.
17) Y. Huang: *J. Appl. Mech.*, **58** (1991), 1084.
18) C. Landron, E. Maire, O. Bouaziz, J. Adrien, L. Lecarme and A. Bareggi: *Acta Mater.*, **59** (2011), 7564.
19) A. Hosokawa, D. S. Wilkinson, J. Kang and E. Maire: *Acta Mater.*, **61** (2013), 1021.
20) A. Hosokawa, D. S. Wilkinson, J. Kang and E. Maire: *Acta Mater.*, **60** (2012), 2829.
21) H. Toda, T. Ohgaki, K. Uesugi, M. Kobayashi, N. Kuroda, T. Kobayashi, M. Niinomi, T. Akahori, K. Makii and Y. Aruga: *Metall. Trans. A*, **37** (2006), 1211.
22) M. Kobayashi, H. Toda, A. Takeuchi, K. Uesugi and Y. Suzuki: *Mater. Charact.*, **69** (2012), 52.
23) D. Seo, F. Tomizato, H. Toda, K. Uesugi, A. Takeuchi, Y. Suzuki and M. Kobayashi: *Appl. Phys. Lett.*, **101** (2012), 261901.
24) M. Kobayashi, H. Toda, Y. Kawai, T. Ohgaki, K. Uesugi, D. S. Wilkinson, T. Kobayashi, Y. Aoki and M. Nakazawa: *Acta Mater.*, **56** (2008), 2167.
25) H. Toda, E. Maire, Y. Aoki and M. Kobayashi: *J. Strain Anal. Eng. Des.*, **46** (2011), 549.
26) W. E. Lorensen and H. E. Cline: *Comput. Graph.*, **21** (1987), 163.
27) P. W. Bridgman: *Rev. Mod. Phys.*, **17** (1945), 3.
28) J. M. Choung and S. R. Cho: *J. Mech. Sci. Technol.*, **22** (2008), 1039.
29) K. S. Zhang and Z. H. Li: *Eng. Fract. Mech.*, **49** (1994), 235.
30) G. LeRoy, J. Embury, G. Edwards and M. F. Ashby: *Acta Metall.*, **29** (1981), 1509.
31) Z. L. Zhang, M. Hauge, J. Ødegård and C. Thaulow: *Int. J. Solids Struct.*, **36** (1999), 3497.
32) A. A. Benzerga, J. Besson and A. Pineau: *Acta Mater.*, **52** (2004), 4623.
33) A. R. Ragab: *Eng. Fract. Mech.*, **71** (2004), 1515.
34) O. Bouaziz, E. Maire, M. Giton, J. Lamarre, Y. Salingue and M. D. Michiele: *Rev. Met. Paris*, **2** (2008), 102.

© 2015 ISIJ